Manuscript version: Published Version

The version presented in WRAP is the published version (Version of Record).

Persistent WRAP URL:

http://wrap.warwick.ac.uk/170566

How to cite:

Please refer to published version for the most recent bibliographic citation information.
If a published version is known of, the repository item page linked to above, will contain
details on accessing it.

Copyright and reuse:

The Warwick Research Archive Portal (WRAP) makes this work by researchers of the
University of Warwick available open access under the following conditions.

Copyright © and all moral rights to the version of the paper presented here belong to the
individual author(s) and/or other copyright owners. To the extent reasonable and
practicable the material made available in WRAP has been checked for eligibility before
being made available.

Copies of full items can be used for personal research or study, educational, or not-for-profit
purposes without prior permission or charge. Provided that the authors, title and full
bibliographic details are credited, a hyperlink and/or URL is given for the original metadata
page and the content is not changed in any way.

Publisher's statement:

Please refer to the repository item page, publisher's statement section, for further
information.

For more information, please contact the WRAP Team at: wrap@warwick.ac.uk.

Ballistic graphene arrays for ultra-high pressure sensing

Abhinaba Sinha,[1] (ID) Pankaj Priyadarshi,[2] (ID) and Bhaskaran Muralidharan[1,a] (ID)

AFFILIATIONS

[1]Department of Electrical Engineering, Indian Institute of Technology Bombay, Powai, Mumbai 400076, India
[2]School of Engineering, University of Warwick, Coventry CV47AL, United Kingdom

[a]Author to whom correspondence should be addressed: bm@ee.iitb.ac.in

ABSTRACT

Atomically thin two-dimensional materials, such as graphene, exhibit extreme high-pressure sensitivity compared to the commercially used pressure sensors due to their high surface-to-volume ratio and excellent mechanical properties. The smaller piezoresistance of graphene across different transport regimes limits its pressure sensitivity compared to other two-dimensional materials. Using membrane theory and the thin-film adhesivity model, we show miniaturization as a means to enhance the overall performance of graphene pressure sensors. Our findings reveal that ballistic graphene can be configured to measure ultra-high pressure ($\approx 10^9$ Pa) with many-fold high-pressure sensitivity than other contemporary two-dimensional materials. Based on these findings, we propose an array of ballistic graphene sensors with extreme high-pressure sensitivity and ultra-high-pressure range that will find applications in next-generation nano-electro-mechanical system pressure sensors. The performance parameters of the array sensors can be further enhanced by reducing the size of graphene membranes and increasing the number of sensors in the array. The methodology developed in this paper can be used to explore similar applications using other two-dimensional materials.

I. INTRODUCTION

The discovery of piezoresistance in silicon and germanium in 1954 laid the foundation for silicon strain gauges.[1] Following this development, the first silicon diaphragm-based pressure sensor was commercially introduced in 1958.[2] Further progress in silicon fabrication processes, such as anisotropic etching,[3–5] ion implantation,[6] anodic bonding,[7,8] and micro-machining processes,[2] paved the way for a reduction in thickness of the membranes and the sensor dimensions. The entire class of sensors that came into being as a result of these developments is known as thin-film micro-electro-mechanical (MEMS) pressure sensors.

Thin-film MEMS pressure sensors are extremely useful for pressure sensing due to their high sensitivity and compact size.[9–11] The mathematical expression for pressure sensitivity (PS) of silicon obtained by Gong and Lee[9] predicts an increase in the PS with the reduction in membrane thickness. Consequently, atomically thin 2D materials are expected to have very high PS and are considered suitable replacements for conventional membranes in pressure sensors. This fact was experimentally confirmed by Smith *et al.*[10] and Wagner *et al.*[11] on graphene and PtSe$_2$, respectively.

Usually, 2D Dirac materials, such as graphene, have a lower gauge factor (GF) than non-Dirac 2D materials, such as layered transition metal dichalcogenides (TMDs), phosphorene, arsenene, and to name a few, due to the presence of robust Dirac cones.[12,13] Hence, non-Dirac 2D materials have higher PS than 2D Dirac materials.[11,14–19] Apart from PS, the performance of a membrane pressure sensor is determined by its yield pressure (P_{yp}, pressure at the yield point)[9] and critical pressure (P_{cr}, the pressure required to delaminate a membrane from the substrate).[20] Among different 2D materials, graphene is considered a strong contender for next-generation pressure sensors because of its high elastic limit (nearly 20%),[21–23] high adhesivity,[20] and high impermeability.[24] Despite the excellent overall properties of graphene, recent studies have shown many-fold higher PS of PtSe$_2$ than graphene[10,11] due to the presence of bandgap in PtSe$_2$.[25]

In this paper, we intend to enhance the PS of graphene further and bring it at par with that of the TMDs. We explore miniaturization as a means to enhance the performance of graphene membranes for next-generation nano-electro-mechanical system (NEMS) pressure sensors. The rapid advancement in the

state-of-the-art lithography techniques has down-scaled MEMS systems to the nanometer range (NEMS).[26] The membrane theory[27,28] and the thin-film adhesivity model[29,30] predict an increase in the magnitude of strain and critical pressure of the membrane, respectively, with dimension reduction. This will lead to an overall performance enhancement and reduction in the dimension of the graphene pressure sensor.

In Secs. II–IV, we develop a theoretical model to calculate the pressure-induced strain within a membrane. Using it, we obtain the PS and pressure range (PR) of graphene membranes in the ballistic, quasi-ballistic, and diffusive regimes. The detailed derivations are given in Appendixes A–E.

II. THEORETICAL MODEL

A. Simulation setup

The schematic diagram of the device setup meant to calculate the PS of graphene is depicted in Fig. 1(a). We use a circular membrane of variable radius a on different substrates to calculate the PS of graphene in different transport regimes, namely, ballistic, quasi-ballistic, and diffusive regimes. The pressure difference (up to 10^9 Pa) applied across the surfaces of the membrane and the corresponding change in electrical resistance due to the deflection are measured [refer to Fig. 1(b)]. The change in resistance with pressure is used to calculate the PS.

B. Pressure sensitivity of graphene

Pressure sensitivity can be expressed as

$$P.S. = GF \times \frac{\varepsilon}{P}, \qquad (1)$$

where GF is the gauge factor, ε is the strain, and P is the pressure difference across the surface (refer to Appendix A). The PS depends on GF and the ratio of strain and pressure. We measure the deflection of the membrane as a function of pressure using membrane theory[27,28] and obtain the strain in the membrane. Using the values of strain as a function of pressure, we calculate the PS using the value of GF of graphene in different transport regimes.[12,13] Graphene has a very low GF across different transport regimes. Thus, the PS of graphene can be increased by increasing the ratio of $\frac{\varepsilon}{P}$.[23] Since the elastic limit of graphene is very high,[23] its
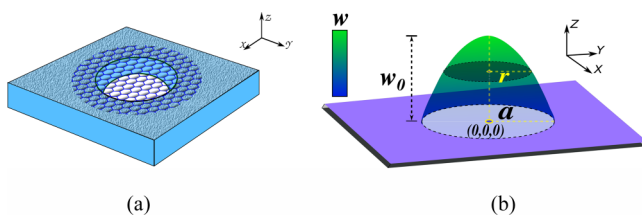
FIG. 1. (a) Schematic diagram for device setup: a circular graphene membrane of radius "a" on different substrates, used to calculate the pressure sensitivity of graphene. (b) Schematic showing a deflected graphene membrane due to an applied pressure across its surfaces.

TABLE I. Comparison of w_0 values obtained here and by Koenig et al.[20]

P (MPa)	w_0 (nm) (this work)	w_0 (nm)[24]
0.145	147	130
0.41	207	220
0.81	260	280

adhesivity with the substrate plays a vital role in defining the maximum PR of the graphene sensor.

In Secs. II B 1–II B 3, we obtain the mathematical expressions for strain as a function of pressure using the deflection of the membrane as a function of pressure. Furthermore, we obtain the critical pressure of graphene membranes of different dimensions on various substrates to find the maximum pressure range.

1. Deflection of membrane

The deflection of the membrane (w) in the z-direction can be approximated [see Fig. 1(b)] as

$$w = w_0 \left(1 - \frac{r^2}{a^2}\right), \qquad (2)$$

where w_0 is the deflection of the center of the membrane, r is the radius of the circle formed in the deflected membrane whose center lies at the coordinates $(0, 0, w)$, and a is the radius of the blister[27] [see Fig. 1(b)]. The value of w_0 can be calculated by applying the principle of virtual displacement and relevant boundary conditions[27,28] (Table I). Thus, the expression for w_0 is given by

$$\frac{w_0}{a} = \left(-\frac{\eta}{2} + \zeta\right)^{\frac{1}{3}} + \left(-\frac{\eta}{2} - \zeta\right)^{\frac{1}{3}}, \qquad (3a)$$

$$\zeta = \sqrt{\left(\frac{\xi}{3}\right)^3 + \left(\frac{\eta}{2}\right)^2}, \qquad (3b)$$

$$\xi = \frac{4}{7 - \gamma}\left(\frac{h}{a}\right)^2, \qquad (3c)$$

$$\gamma = \left\{\frac{3(v-1)}{7-v}\right\}\frac{Pa}{Eh}, \qquad (3d)$$

where v, h, P, and E are, respectively, Poisson's ratio, thickness, pressure, and Young's modulus of the graphene membrane.

2. Strain along the transport direction

An applied pressure across the surface of a circular graphene membrane induces a non-uniform strain. Since we are working in the sheet approximation of graphene (valid for graphene membrane above 100 nm[31] diameter), the strain does not depend on the atomic arrangement.[12,13,32] In order to calculate the PS using uniaxial strain GF,[12,13] we use an approximate method to calculate the strain along the direction of current flow. As the deflections of all
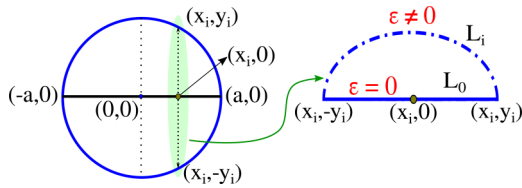
FIG. 2. Schematic representation of methodology for average strain calculation in a deflected membrane. The strain value is averaged over n discrete paths. The top and side views of a single path passing through x_i, 0 are shown.

parallel paths (see Fig. 2), passing through the coordinates $(x_i, 0, 0)$ are different for different values of x_i. Thus, we compute the average uniaxial strain of all these paths. We use a large number of closely spaced paths so that the value of strain converges. The detailed derivation of the expression for average strain along the transport direction is given in Appendix B. The expression for strain is given by

$$\varepsilon_i = \frac{L_i - L_0}{L_0}, \tag{4a}$$

$$\varepsilon_i = \frac{\sqrt{1 + Y^2}}{2} - 1 + \frac{1}{2Y} \log |Y + \sqrt{1 + Y^2}|, \tag{4b}$$

$$\varepsilon_{avg.} = \frac{1}{N} \sum_{i=1}^{N} \varepsilon_i, \tag{4c}$$

where $Y = A y_i$, $A = \frac{-2w_0}{a^2}$, and $y_i = \sqrt{a^2 - x_i^2}$ (see Appendix C for detailed derivation). This approximation gives a quite accurate value of PS since the PS depends on GF [see Eq. (1)], and the values of GF of graphene for different types of strains are very close.[10,12,13,33]

3. Adhesivity of graphene

Graphene is highly adhesive due to its ability to conform to the topography of the substrates.[20] Its high elastic limit[22,23] along with high adhesivity[20,34,35] (see Table II) and impermeability[24] is useful for high-pressure sensing. The maximum PR of graphene depends on its yield-pressure[9] as well as critical pressure.[20]

The PS can be evaluated using Eq. (1), once the ratio of average strain and pressure is obtained from Eq. (4). The critical

TABLE II. Adhesivity of graphene on different substrates.

Substrate	Adhesive energy ($J\,m^{-2}$)	Reference
Ni	72.7	36
Au	7.687	35
Pt	4.021	35
Cu	0.75	34
SiO_2	0.45	20
h$-$BN	0.126	37

pressure of a membrane whose thickness is significantly less than its diameter is given by

$$P_{cr} = \frac{(17.4 E h G_a^3)^{\frac{1}{4}}}{a}, \tag{5}$$

where P_{cr} is the critical pressure, E is Young's modulus, h is the thickness of the membrane, G_a is the adhesivity, and a is the radius of the circular membrane.[29] Using Eq. (5), we obtain the critical pressure of graphene on various substrates. This model accurately predicts the critical pressure of graphene obtained by Koenig et al.[20] The critical pressure obtained experimentally by Koenig et al. for a 2.5 μm radius graphene membrane on SiO_2 is 1.14 MPa, whereas the critical pressure predicted by Eq. (5) is 1.4 MPa, which is pretty close to the experimentally obtained value.

III. RESULTS AND DISCUSSION

The performance of a graphene pressure sensor depends on the membrane material and the substrate. The graphene membrane determines the yield pressure (pressure at the yield point), whereas the substrate's adhesivity determines the critical pressure (minimum pressure required to delaminate graphene from the substrate). Because of the high elastic limit (more than 20%), yield pressure is much larger than the critical pressure in a graphene pressure sensor. Thus, the PR of a graphene sensor depends on its interaction with the substrate.

Figure 3(a) shows an increase in the value of w_0 with an increase in the membrane radius "a," which is evident from Eq. (3). Further, in Fig. 3(b), we observe an increase in the yield pressure with a reduction in the membrane radius. It is because the strain in a deflected membrane is proportional to $\frac{w_0^2}{a^2}$ at a constant pressure[27,28] (see Appendix D) and the value of $\frac{w_0^2}{a^2}$ decreases as
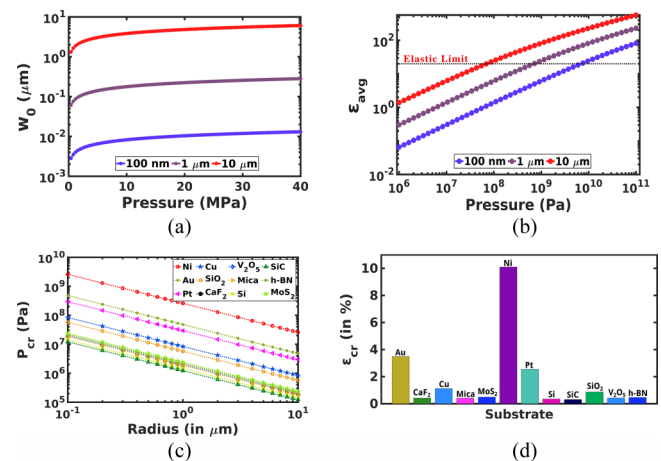
FIG. 3. (a) Displacement of the center of the membrane (w_0) and (b) average strain as a function of pressure for different membrane sizes. (c) Critical pressure of graphene sensors as a function of radius for different substrates. (d) Comparison of the critical strain of graphene on different substrates.

radius "a" decreases [see Fig. 5(a)]. Since the value of yield strain of graphene is independent of its dimension. So, the yield point is reached at a higher pressure when its radius is smaller. The yield pressures of $10\,\mu m$, $1\,\mu m$, and $100\,nm$ are of the order of 10^8, 10^9, and 10^{10} Pa, respectively.

Further, we obtain the critical pressure of graphene from Eq. (5), which is inversely proportional to the radius "a." Consequently, we witness an increase in the critical pressure with the reduction in radius [see Fig. 3(c)]. Figure 3(c) shows the variation of critical pressure as a function of membrane size and substrate. The figure concludes that critical pressure increases 100 times when its radius reduces from $10\,\mu m$ to $100\,nm$. Apart from the radius, the critical pressure of graphene strongly depends on the substrate. In general, graphene is more adhesive to metal substrates, such as nickel, gold, and copper than amorphous insulators, such as SiO_2.[38] Nickel has the highest adhesivity reported so far because of stronger graphene–metal interaction and better lattice match.[39]

From Figs. 3(b) and 3(c), we infer that because of the large yield pressure of graphene, the critical pressure determines the upper limit of the PR. The critical strains of graphene on various substrates are shown in Fig. 3(d). Out of them, graphene has the highest critical strain of $\approx 10\%$ with nickel which is within the linear elastic limit of graphene.[40]

Using Eq. (4), we obtain the PS of ballistic, quasi-ballistic, and diffusive graphene from the values of $\frac{\epsilon}{P}$ and GF in different transport regimes. The value of PS per unit area lies between 10^{-11} and $10^{-10}\,mbar^{-1}\mu m^{-2}$ for diffusive graphene, which is close to the value of PS per unit area obtained by Zhu *et al.*[41] and Wang *et al.*[42] for diffusive graphene. Figure 4 plots the PS per unit area of ballistic, quasi-ballistic, and diffusive graphene and compares their sensitivity with various commercially used membranes. From these plots, we find that ballistic graphene ($a = 100\,nm$) has a very high PS per unit area of nearly $2.5 \times 10^4\,Pa^{-1}\,m^{-2}$. It is approximately 25 times more sensitive than diffusive graphene
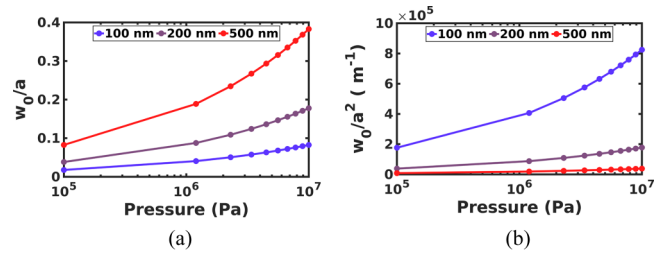
FIG. 5. (a) w_0/a vs pressure (P) and (b) w_0/a^2 vs pressure (P) at different values of membrane radius "a." The value of w_0/a decreases as the radius "a" decreases while w_0/a^2 increases as the radius "a" decreases. Plot (a) implies a reduction in PS with a decrease in radius "a," whereas plot (b) implies an increase in the PS per unit area with a decrease in radius "a."

($10\,\mu m$) and five times more sensitive than quasi-ballistic graphene. The miniaturization of graphene increases its PS per unit area and significantly enhances the PR. The PS per unit area is proportional to $\frac{w_0^2}{a^4}$ (see Appendix D). The value of $\frac{w_0^2}{a^4}$ increases as radius "a" reduces [see Fig. 5(b)]. The maximum pressure that can be sensed using ballistic, quasi-ballistic, and diffusive graphene is of the order of 10^9, 10^8, and 10^7 Pa, respectively.

Despite a very small value of GF,[10,12,13,33] graphene has a significantly higher PS per unit area than silicon (10^3–10^4 times) and GaAs (10^5 times) pressure sensors due to its high surface-to-volume ratio.[10] Hence, other atomically thin 2D materials are also expected to have a high PS like graphene or even more.[11] Among them, TMDs are considered to be the leading contender for replacing graphene due to their high GF (see Table III). Nevertheless, the mechanical properties of graphene are unparalleled, and no other thin-film material could compete with it so far. The excellent adhesivity[24] and mechanical properties[23] of graphene give rise to its high PR. The value of PS per unit area of a 2D sheet of $PtSe_2$, is $10^4\,Pa^{-1}\,m^{-2}$.[11] Figure 4(d) shows that the PS of graphene in the sub-micrometer length scale is comparable to that of the $PtSe_2$, despite the latter having a high GF of -85.[11] Thus, using the miniaturization of graphene, we can design pressure sensors that have a very high PR and high PS.

The higher value of PS per unit area of ballistic graphene does not guarantee higher PS than quasi-ballistic and diffusive graphene due to its smaller surface area. We propose a novel way to overcome this limitation by forming a large array of ballistic graphene nanosensors from a graphene sheet instead of using a single large-sized graphene sensor. By doing so, we effectively increase the overall PS and PR of the graphene sensors. Figures 4(a)–4(c) show the formation of a single pressure sensor of radius $10\,\mu m$ from a $20\,\mu m$ edge square graphene sheet, the formation of an array of pressure sensors of radius $100\,nm$ and $1\,\mu m$ from a 2 and $20\,\mu m$ square graphene sheet, respectively, and the formation of an array of pressure sensors of radius $100\,nm$ from a $20\,\mu m$ square graphene sheet. Note that we consider an ideal case of the sensor array formation from a bigger sheet of graphene, without taking into account the space required for contacts, interconnects, and reference resistors. This assumption
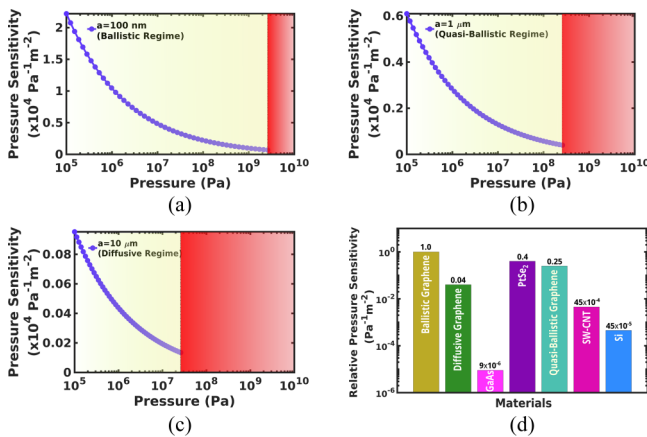
FIG. 4. (a)–(c) Pressure sensitivity per unit area as a function of pressure for membrane radii $100\,nm$, $1\,\mu m$, and $10\,\mu m$ respectively. (d) Comparison of normalized pressure sensitivities of ballistic, quasi-ballistic, and diffusive graphene sensors with commercially used materials.[10,11]

TABLE III. Thickness, Poisson's ratio, Young's modulus, elastic limit, and gauge factor of some common 2D materials.

Materials	h (nm)	ν	E (N/m)	ε (%)	GF
Graphene	0.335[49,52]	0.14[32]	335[53]	>20[23]	0.3–10.3[10,12,13]
Silicene	0.313[54]	0.31[55]	61.33[53]	5[54]	−1.4[56]
Phosphorene	0.9[57]	0.70(zz), 0.18(ac)[58]	92 (zz), 23 (ac)[58,59]	2[60]	120[14,15]
MoS$_2$	0.65[61]	0.25[62]	175.5[63]	3[44]	−148[16]
MoSe$_2$	0.8[64]	0.25[65]	80[45]	2.5[66]	1700[17]
WS$_2$	0.9[67]	0.23[65]	170[68]	2[46]	70[18]
WSe$_2$	1.5[69]	0.21[65]	132.8[70]	2.5[47]	3000[17]
PtSe$_2$	0.507[71]	0.25[48]	58.76[72]	2[48]	−85[11]
ReSe$_2$	0.66[73]	0.223[74]	92.4[74]	3[19]	50,[19] −60[19]

does not affect the relative PS calculation for different cases discussed above as the percentage of sheet area required by the contacts and the reference resistors is the same in each case. The relative PS of array sensors and the pressure sensor formed from the same graphene sheet is shown in Figs. 6(d)–6(f). The relative PS is highest for a 100 nm radius pressure sensor formed from a 20 μm square graphene sheet and is lowest for a 100 nm radius pressure array

formed from a 1 μm square graphene sheet. Hence, we conclude that the smaller the radius of pressure sensors and the larger the size of the graphene sheet, the more is the PS of the system. The advantage of such a system is that a high PS and high PR are simultaneously obtained. Based on these findings, we propose an array sensor of radius 100 nm formed from a large graphene sheet connected to a multi-channel Wheatstone bridge.
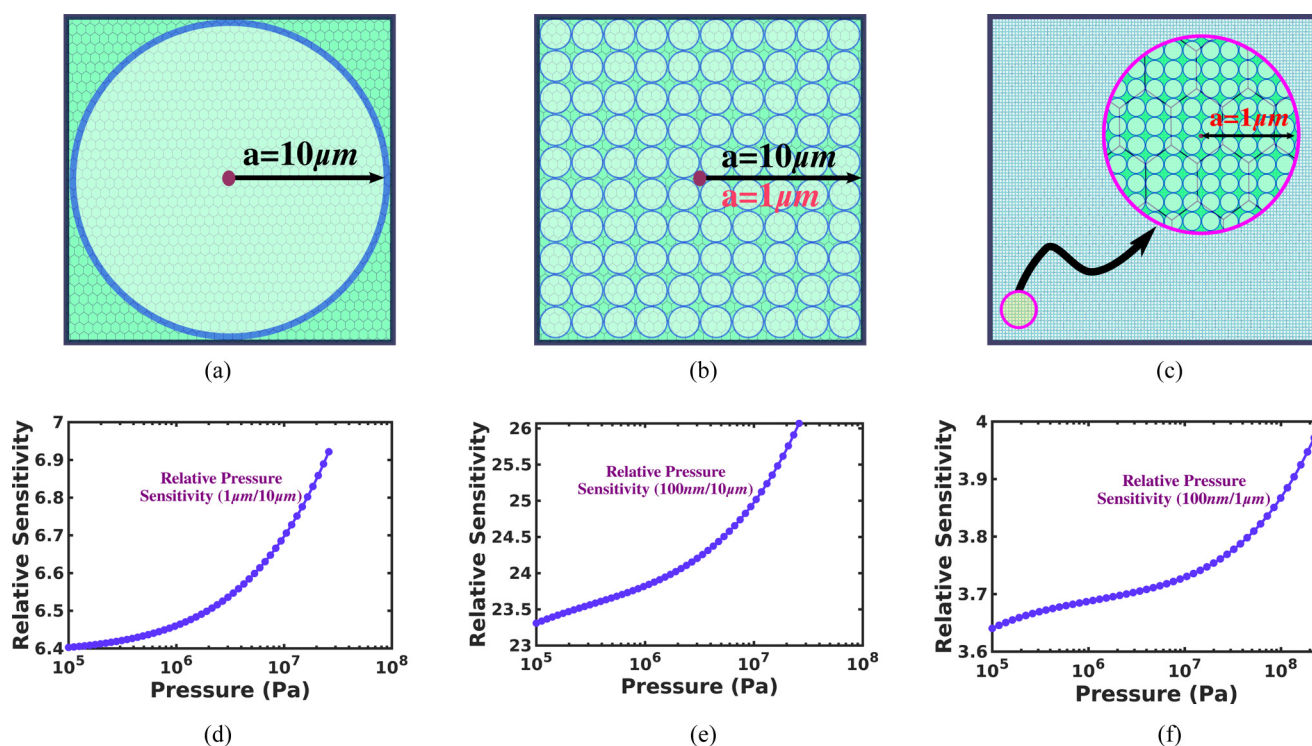

FIG. 6. Schematics representations of: (a) a graphene pressure sensor of radius 10 μm formed from a square sheet of side 20 μm, (b) an array of graphene pressure sensors of radius 100 nm or 1 μm formed from a square sheet of side 2 or 20 μm, respectively, and (c) an array of graphene pressure sensors of radius 100 nm formed from a square graphene sheet of side 20 μm. The ratio of pressure sensitivities of: (d) sensors in sub-figures (b) and (a); (e) sensors of sub-figures (b) and (c); and (f) sensors in sub-figures (c) and (a). *Note:* The percentage of graphene sheet area required for interconnects and reference piezoresistors is assumed to be the same in each case. Hence, relative sensitivity plots in (d)–(f) do not vary with a change in sensor design.

In a n-channel Wheatstone bridge, n-channels or arms are connected in parallel. Out of the n channels, $n - 1$ channels are in an array configuration. Each channel contains a graphene pressure sensor and a reference piezoresistor in series, as shown in Fig. 7(a). The sensors and the reference piezoresistors are identical when the pressure difference is zero across the sensors' surface. The nth channel is the reference channel and has two fixed equivalent resistances in series. When pressure is applied to the sensors, the bridge becomes unbalanced, creating a voltage difference between the sensor (denoted by P) and the reference channels (denoted by P'). The difference signals are fed to an adder to generate a collective array signal.

The inset schematic of Fig. 7(a) shows the magnified view of two adjacent channels of the proposed array sensors' design. The array sensors design consists of $n - 1$ channels on SiO$_2$/Si wafer. The pressure sensor P_n consists of a circular suspended graphene membrane to apply pressure from the bottom. The reference piezoresistor P_n' has a suspended circular graphene membrane placed such that the SiO$_2$ layer is absent, but the silicon layer is present. Other channels

also have the same design. A square-ring-shaped nickel layer is placed across the circular perforation of the pressure sensor. The gaps on the square-ring divide the square nickel substrate. The separated nickel layers do not make any physical contact with each other. The separation between ring is very small and is purposefully done to avoid short-circuit of graphene membrane. The input voltage (V_{in}) and the ground contacts are common for all channels as shown in Fig. 7(a).

The use of array sensors using graphene is highly advantageous. The voltage output of a single graphene pressure sensor of radius $20\,\mu$m is shown in Fig. 7(b), whereas in Fig. 7(c), an array of graphene sensors of radius $1\,\mu$m are shown for $n = 1$ and 100 and in Fig. 7(d), an array of graphene membranes of radius 100 nm are shown for $n = 1$, 100, and 10 000. These figures conclude that the output voltage of smaller-sized sensors when combined in the multi-channel Wheatstone bridge configuration as an array of sensors are many folds more sensitive than a single pressure sensor of equivalent size. We notice a sharp increase in its PR (yellow shaded region) also when multiple smaller sensors are used instead of a single large graphene sensor is used.
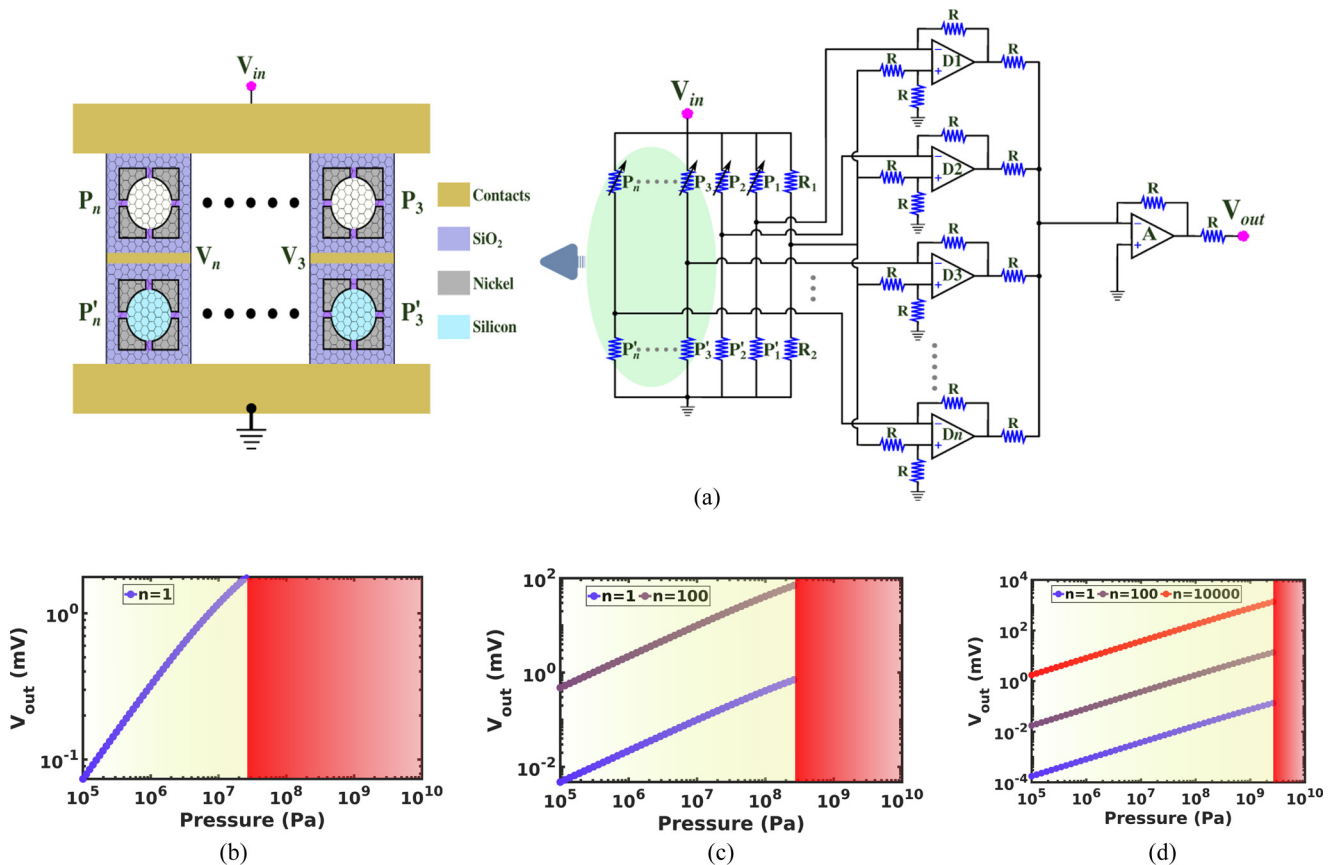
FIG. 7. (a) Circuit diagram of a multi-channel Wheatstone bridge configuration for graphene array pressure sensors. Output voltage (V_{out}) measured using n-channel Wheatstone bridge shown in (a) for different numbers of pressure sensors (n) having radius (b) $10\,\mu$m, (c) $1\,\mu$m, and (d) 100 nm in an array configuration. The output voltage and pressure range (represented by the yellow shaded region) increase by reducing the size of sensors and increasing the number of sensors in the array, keeping the size of the original graphene sheet intact.

The precise fabrication and operation of ballistic graphene pressure sensors are complex despite their numerous advantages. These impediments include diffusion at ultra-high pressure, residual strain in the membrane, and surface defects.

The relation between diffusion flux (J) and pressure gradient across the graphene membrane is given by

$$J = -\frac{D}{k_B T}\frac{dP}{dx};\qquad(6)$$

see Appendix E for a detailed derivation. At a pressure difference of ~100 KPa, the time taken for the gas to leak entirely through monolayer graphene is 72 h.[24] However, at ultra-high pressure (~10^9), the pressure gradient will be significantly high across the graphene membrane. This will lead to rapid gas diffusion through the graphene membrane and possibly destabilize the read-out signal. To avoid this problem, it is necessary to maintain an equilibrium pressure difference across the membrane to facilitate proper PS measurements.

It is pretty evident from Eq. (6) that the flux decreases with an increase in the thickness, i.e., the number of layers of graphene.[24,43] Thus, the diffusion flux may be slightly lower for $PtSe_2$ and other TMDs because of the thicker membrane. Nevertheless, their adhesivity on various substrates[38] and the elastic limit is significantly less compared to graphene.[19,44–48] So, despite a higher GF, the pressure range will be significantly less than graphene. Thus, depending on the requirement, i.e., high PS or ultra-high PR, a trade-off can be made between the membrane's thickness, radius, adhesivity, and GF.

Graphene sensor fabrication involves many complex steps. Therefore, the sensors have surface defects, and residual strain is also present. All these non-ideal conditions affect the overall performance of sensors. The residual strain can usually be removed by applying an offset pressure.

The graphene sensor discussed here is made up of small-sized graphene membranes. Exfoliated graphene flakes are a few hundred nanometers in size and are mostly defect-free.[49] By using exfoliated graphene, we can fabricate ballistic and quasi-ballistic graphene pressure sensors free from surface defects. However, fabricating large arrays of graphene sensors using exfoliated graphene is difficult. One possible way is to fabricate sensor arrays in numerous graphene flakes and integrate them. In the case of graphene sensors using CVD graphene, surface defects are more likely to be present and will affect the sensor's overall performance.

In Fig. 7(a), we see in the inset that graphene sheets are larger than the circular membrane, and the resistance of the graphene on the substrate must be included. This will lead to an increase in the total resistance and reduction in the GF, as the change in resistance will only occur in the circular membrane due to pressure. The mean free path of suspended graphene is larger than graphene on substrates. Therefore, the contact area of graphene on the substrate must be minimum. Graphene on h-BN substrate has a very high mean free path[50] but has a very low adhesivity.[37] Thus, h-BN is a good choice for substrate in graphene pressure sensors when ultra-high PR is not required. For high-pressure sensing, nickel substrate is the best. However, due to the small mean free path of graphene on metals, the graphene–nickel contact area must be small [see Fig. 7(a)]. Graphene has a mean free path of 300 nm on SiO_2. So, the entire setup could

be made on SiO_2/Si wafer as shown in Fig. 7(a), which is conducive for graphene exfoliation as well.

Graphene's ability to sense pressure can be beneficial in many other ways. A pressure sensor transforms pressure waves (sound waves) into electrical signals, similar to how a microphone works. Since graphene microphones have the advantage of being resonance-free in the acoustic range,[51] ballistic graphene array nano-sensors can be instrumental in designing highly sensitive microphones with high pitch and can eventually be useful in modern smartphones.

Apart from this, the methodology used for analyzing ballistic graphene pressure sensors in this paper can be used to explore similar applications in other 2D materials. Among 2D materials, Dirac materials have lower GF than TMDs due to the robust Dirac cones.[17] Hence, it is more likely that nanoscale TMD sheets will have a larger PS than graphene, despite a smaller PR due to the lower elastic limit of TMDs than graphene (see Table III).

IV. CONCLUSION

Motivated by the recent findings that showed the high-pressure sensitivity of atomically thin materials such as graphene, we explored the pressure sensitivity of miniaturized graphene membranes on various substrates using the membrane theory and thin-film adhesivity model. We used these findings on graphene membranes of different dimensions on various substrates and found a 10^3-fold enhancement in the normalized pressure sensitivity per unit area of ballistic graphene compared to commercial silicon pressure sensors. Apart from pressure sensitivity, we showed that ballistic graphene could sense ultra-high pressure of the order of 10^9 Pa. Moreover, we also found that ballistic graphene is 2–3 times more sensitive than TMD, such as $PtSe_2$, despite the latter having a much higher gauge factor compared to graphene. Finally, this paper concludes that a ballistic graphene pressure sensor is a perfect blend of high-pressure sensitivity and ultra-high pressure range. Based on these results, we proposed ballistic graphene array sensors as next-generation NEMS pressure sensors for ultra-high pressure sensing.

AUTHOR DECLARATIONS
Conflict of Interest

The authors have no conflicts to disclose.

Author Contributions

Abhinaba Sinha: Conceptualization (lead); Data curation (lead); Formal analysis (lead); Investigation (lead); Methodology (lead);

Validation (equal); Writing – original draft (lead); Writing – review & editing (equal). **Pankaj Priyadarshi:** Resources (supporting); Software (supporting). **Bhaskaran Muralidharan:** Funding acquisition (equal); Supervision (equal); Writing – review & editing (equal).

DATA AVAILABILITY

The data that support the findings of this study are available within the article.

APPENDIX A: EXPRESSION FOR PRESSURE SENSITIVITY

Pressure sensitivity is expressed as

$$PS = \frac{\Delta R/R_0}{P}, \tag{A1}$$

where ΔR is the change in resistance due to pressure P and R_0 is the resistance of membrane at zero strain. The right hand side of Eq. (A1) can be written as $\frac{\Delta R}{\varepsilon R_0} \times \frac{\varepsilon}{P}$. The quantity ε is the strain generated in the membrane due to pressure (P) and $\frac{\Delta R}{\varepsilon R_0}$ is the gauge factor (GF). Thus, Eq. (A1) simplifies into

$$PS = GF \times \frac{\varepsilon}{P}. \tag{A2}$$

APPENDIX B: DEFLECTION OF MEMBRANE

The pressure difference across the top and bottom surfaces causes the membrane to deflect [see Fig. 1(b)]. The large scale deflection of the membrane is approximated by the expression

$$w = w_0\left(1 - \frac{r^2}{a^2}\right). \tag{B1}$$

The radial displacement (u) can be approximately written as

$$u = r(a - r)(c_1 + rc_2), \tag{B2}$$

where c_1 and c_2 are constant. The value of w_0 can be easily computed using the principle of virtual displacement. According to this principle, change in mechanical energy is equal to work done by the pressure to deflect the membrane.[28] The mechanical energy of a membrane includes strain energy and bending energy. On solving the value of w_0 using this principle, we obtain an analytical expression of w_0 as a function of applied pressure, thickness, and radius of the membrane.[27,28]

The value of strain energy of a circular membrane is given by

$$V_s = \pi K \int_0^a \left(\varepsilon_r^2 + \varepsilon_\theta^2 + 2\nu\varepsilon_r + \varepsilon_\theta\right) r\,dr, \tag{B3a}$$

$$K = \frac{Eh}{1 - \nu^2}, \tag{B3b}$$

$$\varepsilon_r = \frac{du}{dr} + \frac{1}{2}\left(\frac{dw}{dr}\right)^2, \tag{B3c}$$

$$\varepsilon_\theta = \frac{u}{r}. \tag{B3d}$$

On simplifying the above equations, we obtain the strain energy as

$$V_s = \frac{\pi Eh}{1 - \nu^2}\left[\frac{1}{4}c_1^2 a^4 + \frac{3}{10}c_1 c_2 a^5 - \frac{1}{5}(3 - \nu)c_1 a w_0^2 \right.$$
$$\left. + \frac{7}{60}c_2^2 a^6 - \frac{2}{15}(3 - \nu)c_2 a^2 w_0^2 + \frac{2}{3}\frac{w_0^4}{a^2}\right]. \tag{B4}$$

The bending strain energy of a membrane is given by[28]

$$V_b = 4\pi D(1 + \nu)\left(\frac{w_0}{a}\right)^2, \tag{B5}$$

where $D = \frac{Eh^3}{12(1-\nu^2)}$ is the bending rigidity. The work done by the pressure to deflect the circular membrane is given by[27]

$$W = \frac{\pi a^2 P}{2}w_0. \tag{B6}$$

In equilibrium, the value of V_s is minimum with respect to c_1 and c_2. Using these conditions along with the principle of virtual displacement,[28] we obtain the value of w_0. These conditions are mathematically expressed as

$$\frac{dV_s}{dc_1} = \frac{dV_s}{dc_2} = 0, \tag{B7a}$$

$$\frac{d(V_s + V_b)}{dw_0}\delta w_0 = \frac{dW}{dw_0}\delta w_0. \tag{B7b}$$

On solving Eq. (B7), we obtain a cubic equation in terms of w_0 which is given by[27]

$$w_0^3 + \frac{4h^2}{(7 - \nu)}w_0 - \frac{3(1 - \nu)Pa^4}{Eh} = 0. \tag{B8}$$

Solving Eq. (B8) using Cardan's formula, we get the value of w_0 required in Eq. (2).

APPENDIX C: STRAIN ALONG THE TRANSPORT DIRECTION

The strain (ε) along the transport direction is different at different portions of the circular membrane, as shown in Fig. 2. Thus, we have to calculate the average strain in the membrane due to applied pressure. We divide the circular basement of the deflected membrane into a large number of parallel chord paths along the transport direction. The strain in the geodesic arcs of the deflected membrane along these chord paths are given by the difference in the length of the geodesic arc and the length of the corresponding chords.

The length of the chord in an unstrained membrane passing through $(x_i, 0, 0)$ is equal to $L_0 = \sqrt{a^2 - x_i^2}$. The length of the line passing through the deflected surface is given by

$$L_i = \int_0^{\sqrt{a^2 - x_i^2}} \sqrt{1 + \left(\frac{dw}{dy}\right)^2}\, dy. \tag{C1}$$

The value of strain ε_i can be written as

$$\varepsilon_i = \frac{L_i - L_0}{L_0}. \tag{C2}$$

On simplification of Eq. (C1) using Eq. (B1), we obtain

$$L_i = \frac{Y\sqrt{1 + Y^2}}{2A} + \frac{1}{2A}\log|Y + \sqrt{1 + Y^2}|, \tag{C3}$$

where $Y = -\frac{-2w_0\sqrt{a^2 - x_i^2}}{a^2}$ and $A = \frac{-2w_0}{a^2}$. Further, using Eqs. (C2) and (C3), we obtain the strain along the direction of transport.

APPENDIX D: PRESSURE SENSITIVITY PER UNIT AREA OF GRAPHENE MEMBRANE

The PS of a graphene membrane is given by Eq. (1). The GF of graphene is very small across different length scales due to the presence of robust Dirac cones.[12,13] According to Eq. (1), PS depends on the magnitude of strain at a particular pressure. The radial (ε_r) and tangential strains (ε_θ) are expressed as

$$\varepsilon_r = \frac{3 - v}{4}\left(\frac{w_0}{a}\right)^2\left[1 - \frac{1 - 3v}{3 - v}\left(\frac{r}{a}\right)^2\right] \tag{D1a}$$

and

$$\varepsilon_\theta = \frac{3 - v}{4}\left(\frac{w_0}{a}\right)^2\left[1 - \left(\frac{r}{a}\right)^2\right], \tag{D1b}$$

respectively,[27] where v is Poisson's ratio. At any point in the deflected membrane, strain components are directly proportional to $\frac{w_0^2}{a^2}$. Thus, PS is directly proportional to $\frac{w_0^2}{a^2}$, and PS per unit area is directly proportional to $\frac{w_0^2}{a^4}$.

APPENDIX E: EXPRESSION FOR DIFFUSION THROUGH GRAPHENE

The ideal gas equation is given by

$$PV = Nk_B T, \tag{E1}$$

where N is the number of gas molecules, k_B is the Boltzmann constant, P is the pressure, V is the volume, and T is the temperature. Equation (E1) can be written as

$$P = \phi k_B T, \tag{E2}$$

where ϕ is the concentration of gas. Using Fick's law, we can write the diffusion flux as

$$F = -D\frac{d\phi}{dx}. \tag{E3}$$

Here, D is the diffusion coefficient of gas and F is the gas flux. From Eqs. (E2) and (E3), we obtain the relation between gas flux and pressure gradient across graphene (assuming T is constant). The mathematical relation between these quantities is given by

$$F = -\frac{D}{k_B T}\frac{d\phi}{dx}. \tag{E4}$$

REFERENCES

[1]C. S. Smith, Phys. Rev. **94**, 42 (1954).
[2]J. Bryzek, "Silicon sensors and microstructures," in *Electro International, 1991* (IEEE, 1991), pp. 661–665.
[3]D. L. Kendall, Appl. Phys. Lett. **26**, 195 (1975).
[4]K. E. Bean, IEEE Trans. Electron Devices **25**, 1185 (1978).
[5]E. Bassous, IEEE Trans. Electron Devices **25**, 1178 (1978).
[6]S. K. Gandhi and V. F. Principles, *VLSI Fabrication: Silicon and Gallium Arsenide* (Wiley, 1983).
[7]D. I. Pomerantz, "Anodic bonding," U.S. patent 3,397,278 (1968).
[8]G. Wallis and D. I. Pomerantz, J. Appl. Phys. **40**, 3946 (1969).
[9]S.-C. Gong and C. Lee, IEEE Sens. J. **1**, 340 (2001).
[10]A. Smith, F. Niklaus, A. Paussa, S. Vaziri, A. C. Fischer, M. Sterner, F. Forsberg, A. Delin, D. Esseni, P. Palestri, M. Östling, and M. C. Lemme, Nano Lett. **13**, 3237 (2013).
[11]S. Wagner, C. Yim, N. McEvoy, S. Kataria, V. Yokaribas, A. Kuc, S. Pindl, C.-P. Fritzen, T. Heine, G. S. Duesberg, and M. C. Lemme, Nano Lett. **18**, 3738 (2018).
[12]A. Sinha, A. Sharma, A. Tulapurkar, V. R. Rao, and B. Muralidharan, Phys. Rev. Mater. **3**, 124005 (2019).
[13]A. Sinha, A. Sharma, P. Priyadarshi, A. Tulapurkar, and B. Muralidharan, Phys. Rev. Res. **2**, 043041 (2020).
[14]Z. Zhang, L. Li, J. Horng, N. Z. Wang, F. Yang, Y. Yu, Y. Zhang, G. Chen, K. Watanabe, T. Taniguchi, X. H. Chen, F. Wang, and Y. Zhang, Nano Lett. **17**, 6097 (2017).
[15]Z. Nourbakhsh and R. Asgari, Phys. Rev. B **98**, 125427 (2018).
[16]S. Manzeli, A. Allain, A. Ghadimi, and A. Kis, Nano Lett. **15**, 5330 (2015).
[17]M. Hosseini, M. Elahi, M. Pourfath, and D. Esseni, Appl. Phys. Lett. **107**, 253503 (2015).
[18]W. Zhang, R. Frisenda, Q. Zhao, F. Carrascoso, A. Al-Enizi, A. Nafady, and A. Castellanos-Gomez, Sens. Actuat. A: Phys. **332**, 113204 (2021).
[19]C. An, Z. Xu, W. Shen, R. Zhang, Z. Sun, S. Tang, Y.-F. Xiao, D. Zhang, D. Sun, X. Hu, C. Hu, L. Yang, and J. Liu, ACS Nano **13**, 3310 (2019).
[20]S. P. Koenig, N. G. Boddeti, M. L. Dunn, and J. S. Bunch, Nat. Nanotechnol. **6**, 543 (2011).
[21]S. Ogata and Y. Shibutani, Phys. Rev. B **68**, 165409 (2003).
[22]F. Liu, P. Ming, and J. Li, Phys. Rev. B **76**, 064120 (2007).
[23]C. Lee, X. Wei, J. W. Kysar, and J. Hone, Science **321**, 385 (2008).
[24]J. S. Bunch, S. S. Verbridge, J. S. Alden, A. M. van der Zande, J. M. Parpia, H. G. Craighead, and P. L. McEuen, Nano Lett. **8**, 2458 (2008).
[25]Y. Wang, L. Li, W. Yao, S. Song, J. T. Sun, J. Pan, X. Ren, C. Li, E. Okunishi, Y.-Q. Wang, E. Wang, Y. Shao, Y. Y. Zhang, H.-T. Yang, E. F. Schwier, H. Iwasawa, K. Shimada, M. Taniguchi, Z. Cheng, S. Zhou, S. Du, S. J. Pennycook, S. T. Pantelides, and H.-J. Gao, Nano Lett. **15**, 4013 (2015).
[26]J. D. Plummer, *Silicon VLSI Technology: Fundamentals, Practice and Modeling* (Pearson Education India, 2009).
[27]F. Zhao, in *Modeling, Signal Processing, and Control for Smart Structures 2008*, International Society for Optics and Photonics Vol. 6926, edited by D. K. Lindner (SPIE, 2008), pp. 232–243.

[28]S. Timoshenko and S. Woinowsky-Krieger, *Theory of Plates and Shells* (McGraw Hill, 1959).

[29]A. Gent and L. Lewandowski, J. Appl. Polym. Sci. **33**, 1567 (1987).

[30]K. B. Liland, H. Faremo, and K.-M. Furuheim, in *Proceedings of the Nordic Insulation Symposium* (2019), Vol. 26, pp. 108–112.

[31]M. Y. Han, B. Özyilmaz, Y. Zhang, and P. Kim, Phys. Rev. Lett. **98**, 206805 (2007).

[32]R. M. Ribeiro, V. M. Pereira, N. M. R. Peres, P. R. Briddon, and A. H. C. Neto, New J. Phys. **11**, 115002 (2009).

[33]A. D. Smith, F. Niklaus, A. Paussa, S. Schröder, A. C. Fischer, M. Sterner, S. Wagner, S. Vaziri, F. Forsberg, D. Esseni, M. Östling, and M. C. Lemme, ACS Nano **10**, 9879 (2016).

[34]T. Yoon, W. C. Shin, T. Y. Kim, J. H. Mun, T.-S. Kim, and B. J. Cho, Nano Lett. **12**, 1448 (2012).

[35]J. Torres, Y. Zhu, P. Liu, S. C. Lim, and M. Yun, Physica Status Solidi A **215**, 1700512 (2018).

[36]S. Das, D. Lahiri, D.-Y. Lee, A. Agarwal, and W. Choi, Carbon **59**, 121 (2013).

[37]E. Khestanova, F. Guinea, L. Fumagalli, A. Geim, and I. Grigorieva, Nat. Commun. **7**, 1 (2016).

[38]Y. T. Megra and J. W. Suk, J. Phys. D: Appl. Phys. **52**, 364002 (2019).

[39]Y. Gamo, A. Nagashima, M. Wakabayashi, M. Terai, and C. Oshima, Surf. Sci. **374**, 61 (1997).

[40]V. M. Pereira, A. H. Castro Neto, and N. M. R. Peres, Phys. Rev. B **80**, 045401 (2009).

[41]S.-E. Zhu, M. Krishna Ghatkesar, C. Zhang, and G. C. A. M. Janssen, Appl. Phys. Lett. **102**, 161904 (2013).

[42]Q. Wang, W. Hong, and L. Dong, Nanoscale **8**, 7663 (2016).

[43]C. Sun and B. Bai, Appl. Therm. Eng. **116**, 724 (2017).

[44]Q. Peng and S. De, Phys. Chem. Chem. Phys. **15**, 19427 (2013).

[45]X. Wang, Y. Hong, M. Wang, G. Xin, Y. Yue, and J. Zhang, Phys. Chem. Chem. Phys. **21**, 9159 (2019).

[46]S. Deng, L. Li, and M. Li, Physica E **101**, 44 (2018).

[47]W. Ding, D. Han, J. Zhang, and X. Wang, Mater. Res. Express **6**, 085071 (2019).

[48]J. Du, P. Song, L. Fang, T. Wang, Z. Wei, J. Li, and C. Xia, Appl. Surf. Sci. **435**, 476 (2018).

[49]K. S. Novoselov, A. K. Geim, S. V. Morozov, D. Jiang, Y. Zhang, S. V. Dubonos, I. V. Grigorieva, and A. A. Firsov, Science **306**, 666 (2004).

[50]C. R. Dean, A. F. Young, I. Meric, C. Lee, L. Wang, S. Sorgenfrei, K. Watanabe, T. Taniguchi, P. Kim, K. L. Shepard, and J. Hone, Nat. Nanotechnol. **5**, 722 (2010).

[51]S. Wittmann, C. Glacer, S. Wagner, S. Pindl, and M. C. Lemme, ACS Appl. Nano Mater. **2**, 5079 (2019).

[52]A. H. Castro Neto, F. Guinea, N. M. R. Peres, K. S. Novoselov, and A. K. Geim, Rev. Mod. Phys. **81**, 109 (2009).

[53]R. John and B. Merlin, Cryst. Struct. Theor. Appl. **5**, 43 (2016).

[54]Q. Peng, X. Wen, and S. De, RSC Adv. **3**, 13772 (2013).

[55]R. Qin, W. Zhu, Y. Zhang, and X. Deng, Nanoscale Res. Lett. **9**, 1 (2014).

[56]S. Sahoo, A. Sinha, N. A. Koshi, S. Lee, S. Bhattacharjee, and B. Muralidharan, J. Phys. D: Appl. Phys. **55**, 425301 (2022).

[57]H. Liu, A. T. Neal, Z. Zhu, Z. Luo, X. Xu, D. Tománek, and P. D. Ye, ACS Nano **8**, 4033 (2014).

[58]L. Wang, A. Kutana, X. Zou, and B. I. Yakobson, Nanoscale **7**, 9746 (2015).

[59]Q. Wei and X. Peng, Appl. Phys. Lett. **104**, 251915 (2014).

[60]G. Liu, Z. Gao, and J. Zhou, Physica E **112**, 59 (2019).

[61]X. Li and H. Zhu, J. Materiom. **1**, 33 (2015).

[62]J. Kang, H. Sahin, and F. M. Peeters, Phys. Chem. Chem. Phys. **17**, 27742 (2015).

[63]S. Bertolazzi, J. Brivio, and A. Kis, ACS Nano **5**, 9703 (2011).

[64]X. Lu, M. I. B. Utama, J. Lin, X. Gong, J. Zhang, Y. Zhao, S. T. Pantelides, J. Wang, Z. Dong, Z. Liu, W. Zhou, and Q. Xiong, Nano Lett. **14**, 2419 (2014).

[65]Y. Yoo, J.-H. Yang, and J.-H. Lee, Curr. Appl. Phys. **18**, 799 (2018).

[66]Y. Yang, X. Li, M. Wen, E. Hacopian, W. Chen, Y. Gong, J. Zhang, B. Li, W. Zhou, P. M. Ajayan *et al.*, Adv. Mater. **29**, 1604201 (2017).

[67]J. Park, M. S. Kim, E. Cha, J. Kim, and W. Choi, Sci. Rep. **7**, 1 (2017).

[68]K. Liu, Q. Yan, M. Chen, W. Fan, Y. Sun, J. Suh, D. Fu, S. Lee, J. Zhou, S. Tongay, J. Ji, J. B. Neaton, and J. Wu, Nano Lett. **14**, 5097 (2014).

[69]J.-W. Chen, S.-T. Lo, S.-C. Ho, S.-S. Wong, X.-Q. Zhang, Y.-D. Liu, Y.-Y. Chiou, Y.-X. Chen, J.-C. Yang, Y.-C. Chen *et al.*, Nat. Commun. **9**, 1 (2018).

[70]F. Zeng, W.-B. Zhang, and B.-Y. Tang, Chin. Phys. B **24**, 097103 (2015).

[71]G. Kliche, J. Solid State Chem. **56**, 26 (1985).

[72]S. Deng, L. Li, and Y. Zhang, ACS Appl. Nano Mater. **1**, 1932 (2018).

[73]S. Yang, S. Tongay, Y. Li, Q. Yue, J.-B. Xia, S.-S. Li, J. Li, and S.-H. Wei, Nanoscale **6**, 7226 (2014).

[74]H. Wang, E. Liu, Y. Wang, B. Wan, C.-H. Ho, F. Miao, and X. G. Wan, Phys. Rev. B **96**, 165418 (2017).